crystals

MDPI

*Article*

# Innovative Dual-Functional Photocatalyst Design for Precision Water Remediation

**Yike Li [1,*] and Xian Liu [2,*]**

[1] School of Civil Engineering and Architecture, Wuhan University of Technology, Wuhan 430070, China
[2] School of Urban Construction, Wuhan University of Science and Technology, Wuhan 430065, China
* Correspondence: 17786380969@163.com (Y.L.); xianliu@wust.edu.cn (X.L.)

**Abstract:** This study pioneers the development of a synergistic Ag-doped molecularly imprinted $TiO_2$ photocatalyst (MIP-Ag-$TiO_2$) through a multi-strategy engineering approach, integrating molecular imprinting technology with plasmonic metal modification via a precisely optimized sol–gel protocol. Breaking from conventional non-selective photocatalysts, our material features an engineered surface architecture that combines selective molecular recognition sites with enhanced charge separation capabilities, specifically tailored for the targeted degradation of recalcitrant salicylic acid (SA) contaminants. Advanced characterization (XRD, EPR, FT-IR, TEM-EDS) reveals unprecedented structure–activity relationships, demonstrating how template molecule ratios (Ti:SA = 5:1) and calcination parameters (550 °C) collaboratively optimize both adsorption selectivity and quantum efficiency. The optimized MIP-Ag-$TiO_2$ achieves breakthrough performance metrics: 98.6% SA degradation efficiency at 1% Ag doping, coupled with a record selectivity coefficient R = 7.128. Mechanistic studies employing radical trapping experiments identify a dual $\bullet OH/O_2^-$-mediated degradation pathway enabled by the Ag-$TiO_2$ Schottky junction. This work establishes a paradigm-shifting "capture-and-destroy" photocatalytic system that simultaneously addresses the critical challenges of selectivity and quantum yield limitations in advanced oxidation processes, positioning molecularly imprinted plasmonic photocatalysts as next-generation smart materials for precision water purification.

**Keywords:** photocatalysis; titanium dioxide; Ag doping; molecular imprinting; salicylic acid

check for updates

Academic Editor: Nabeen K Shrestha

Received: 14 April 2025
Revised: 17 May 2025
Accepted: 19 May 2025
Published: 21 May 2025

**Citation:** Li, Y.; Liu, X. Innovative Dual-Functional Photocatalyst Design for Precision Water Remediation. *Crystals* **2025**, *15*, 483. https://doi.org/10.3390/cryst15050483

**Copyright:** © 2025 by the authors. Licensee MDPI, Basel, Switzerland. This article is an open access article distributed under the terms and conditions of the Creative Commons Attribution (CC BY) license (https://creativecommons.org/licenses/by/4.0/).

## 1. Introduction

With the rapid development of industrialization and urbanization, the types and concentrations of organic pollutants in water bodies have been continuously increasing [1], posing serious threats to the ecological environment and human health [2]. Photocatalytic technology, due to its high efficiency and environmental friendliness, has become an effective method for degrading organic pollutants [3]. In the field of environmental treatment technology, titanium-based semiconductor materials have long dominated by virtue of their unique physicochemical properties. In particular, the titanium dioxide ($TiO_2$) system has been applied in industrial photocatalysis for decades due to its excellent light corrosion resistance, excellent thermal stability, and significant economic advantages. However, as the demand for environmental pollution treatment develops in the direction of precision and diversification, the technological bottleneck of traditional photocatalytic systems in molecular recognition and targeted conversion has become more and more prominent [3].

The core challenge in the field of environmental remediation is that the recognition selectivity and conversion efficiency of heterogeneous photocatalytic systems for specific

pollutants in complex media struggle to meet the actual needs. When dealing with complex pollution systems containing multiple organic pollutants, heavy metal ions, and pathogenic microorganisms, traditional $TiO_2$-based materials often exhibit non-selective broad-spectrum degradation, which not only results in the loss of energy efficiency but also leads to the generation of secondary pollutants. This technical shortcoming is particularly prominent in the treatment scenario of difficult-to-degrade pollutants such as salicylic acid wastewater [4].

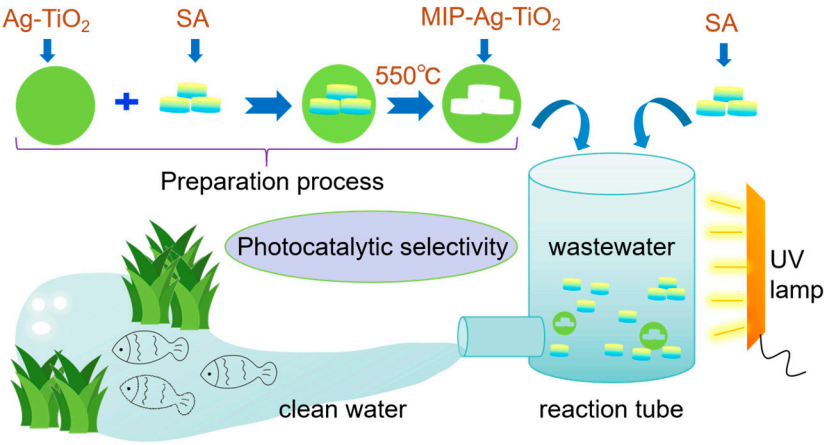
SA is an important metabolite of aspirin and is widely used as a pain reliever to prevent heart attacks, as a preservative in food and cosmetics, and for the treatment of keratosis and dermatitis [5]. The structural formula of SA is HO-$C_6H_4$-COOH, where -OH and -COOH are in neighboring positions, meaning it is called "O-hydroxybenzoic acid". SA is stable at room temperature and decomposes to phenol and carbon dioxide under rapid heating [6]. Gu Xiaoxue et al. [7] used urea and lanthanum nitrate as precursors to prepare N, La co-doped $TiO_2$ photocatalysts by the sol–gel method, and the removal rate of SA was up to 98.18% at 60 min when the doping ratio N:La was 40:0.1, while the removal rate of $TiO_2$ was only 50%. This result indicates that SA can be efficiently removed in a shorter time by the improved photocatalytic oxidation method, which is more effective than the traditional physicochemical or biological methods.

Based on this, the international academic community is working on the development of fourth-generation smart photocatalytic material systems. The research focuses on three dimensions: firstly, the electronic structure of the material surface is regulated by crystal engineering to construct active sites with a molecular recognition function; secondly, the development of a multivariate heterojunction system serves to enhance the carrier separation efficiency by utilizing the synergistic effect of energy bands; and lastly, the temporal and spatial coupling of pollutant-specific adsorption and photocatalytic degradation is realized by combining molecular imprinting technology [8].

Molecularly imprinted technology (MIP) can significantly enhance material selectivity by forming specific recognition sites on the material surface through template molecules [9]. Meanwhile, noble metal doping (such as silver) can improve the light absorption properties and charge separation efficiency of $TiO_2$ [10], thereby enhancing its photocatalytic activity [11]. This study aimed to combine molecularly imprinted technology with silver doping to synthesize a novel silver-doped molecularly imprinted titanium dioxide (MIP-Ag-$TiO_2$) material for the efficient and selective degradation of salicylic acid (SA) [12]. This study advances efficient photocatalyst design through optimized synthesis and structure–performance analysis. Using salicylic acid (SA)—a common pharmaceutical pollutant with coexisting hydroxyl/carboxylic groups on its benzene ring—as a model target, the work addresses the low degradation efficiency of traditional systems. SA was selected for its frequent detection in drinking water and as a probe to validate a dual enhancement strategy: Molecularly imprinted cavities spatially match SA's molecular size for selective adsorption; Ag nanoparticle integration creates localized field effects that specifically activate SA's carboxylic acid group. This synergy between precise molecular recognition and targeted energy delivery demonstrates a blueprint for developing pollutant-specific photocatalytic systems.

This work developed MIP-Ag-$TiO_2$ via sol–gel synthesis, optimizing the calcination temperature, template molecule dosage, and Ag doping ratio to achieve 98.6% SA degradation (Scheme 1). Combining molecular imprinting and Ag plasmonic activation, the material overcomes traditional photocatalysts' limitations in selectivity and light response: Targeted recognition: Imprinted cavities selectively adsorb SA via size matching. Precision activation: Ag nanoparticles enhance localized fields to break SA's carboxylic bonds. Characterized by XRD, BET, EPR, FT-IR, XPS UV-vis, and TEM-EDS, the optimized

system demonstrates an unparalleled SA removal efficiency and selectivity (under UV light). This dual-functional "recognition–activation" design establishes a groundbreaking strategy for smart environmental materials, advancing the precision remediation of refractory pollutants.




**Scheme 1.** Preparation of MIP-Ag-$TiO_2$ and schematic diagram for photocatalytic selective degradation of wastewater.

## 2. Materials and Methods

### *2.1. Preparation and Characterization of Ag-Doped Molecularly Imprinted $TiO_2$*

Molecularly imprinted photocatalysts have been prepared for wastewater treatment, but there is a lack of Ag-doped molecularly imprinted photocatalysts reported for salicylic acid. The MIP-Ag-$TiO_2$ catalysts were synthesized by dissolving tetra-n-butyl titanate (20 mL) in ethanol (40 mL) and acetic acid (10 mL), followed by adding salicylic acid (Ti:SA = 4:1, 5:1, 6:1) to form Solution A. Solution B was prepared by dissolving $AgNO_3$ (0%, 1%, 2%) in ethanol (40 mL) with deionized water (1 mL). Solution B is added slowly with stirring (500 rpm) to Solution A. Stirring was continued for 2 h after the dropping was finished, and then the stirring was stopped and the catalyst was aged at room temperature for 24 h. Drying in an oven at 80 °C for 10 h yielded a bulk solid, which was ground to fine particles and then calcined at 450 °C, 550 °C, or 650 °C for 2 h to yield the final catalyst. This method ensured we had precise control of silver loading, molecular imprinting, and crystallinity.

Comparison of catalyst preparation methods.: Repeating the above steps, Ag-$TiO_2$ can be obtained when SA is not added to Solution A. MIP-$TiO_2$ can be obtained when $AgNO_3$ is not added to Solution B. When SA is not added to liquid A and $AgNO_3$ is not added to Solution B, MIP-$TiO_2$ can be obtained.

### *2.2. Characterization of the Material Properties of Catalysts*

Using a gold-sputtered electrode, the powder was directly adhered to conductive tape to measure the field-emission scanning electron microscopy (SEM, Oxford ULTIM MAX 40, Oxfordshire, UK) morphology in secondary electron mode (acceleration voltage: 5 kV, working distance: 6 mm, beam current: 100 pA, vacuum: $5 \times 10^{-4}$ Pa, image resolution: 1024 × 884 pixels). Field-emission transmission electron microscopy (TEM, JEOL JEM-2100F, Tokyo, Japan) was employed to test the energy-dispersive X-ray spectroscopy (EDS) mapping and morphology, with a standard carbon film grid used for sample preparation. The sample was ultrasonicated in ethanol for 5 min. The phase composition of the catalyst was analyzed using an X-ray diffractometer (XRD, Bruker D8 Advanced, Karlsruhe, Germany) with a scanning speed of 5°/min and a testing range of 5° to 90°. The elemental

composition of the sample was determined using X-ray photoelectron spectroscopy (XPS, Thermo SCIENTIFIC ESCALAB 250Xi, Waltham, MA, USA). X-ray source parameters: A monochromatized Al Kα X-ray source (energy = 1486.6 eV) was used with a power setting of 150 W (voltage 15 kV, beam current 10 mA) and a beam spot size of 500 μm. Analyzer type and settings: A Hemispherical Energy Analyzer (HSA) in the working mode was used as a fixed analyzer of transfer energy (CAE mode). Ultraviolet-visible (UV-Vis) spectra in the range of 200–800 nm were measured in diffuse reflectance mode using a UV-Vis spectrophotometer (PerkinElmer LAMBDA 1050+, Shelton, CT, USA). Fourier-transform infrared spectroscopy (FT-IR) was performed using a Bruker 70 V spectrometer. In situ electron paramagnetic resonance (EPR, Bruker A300, Billerica, MA, USA) was employed to test the free radicals in the catalyst under 365 nm ultraviolet light excitation at room temperature. 5,5-Dimethyl-1-pyrroline N-oxide (DMPO) was used as the spin-trapping agent. After ultrasonic dispersion in 1 mL of methanol, 200 μL of the solution was mixed with an equal volume of DMPO solution, and the mixture was tested under both dark and illuminated conditions to detect •OH, $h^+$, and $\bullet O_{2^-}$ radicals.

### *2.3. Photocatalytic Degradation Experiments of Ag-Doped Molecularly Imprinted $TiO_2$*

The photocatalytic degradation process can be evaluated through the absorbance index, which serves as a fundamental metric for assessing photocatalytic efficacy [13].

At the beginning of the experiment, comparative adsorption performance experiments were conducted for all catalysts, i.e., stirring under dark conditions for 30 min and sampling at different moments to test the change in concentration of the stock solution.

A quantity of 0.06 g of photocatalyst, adhering to the standard addition protocol, is introduced into 60 mL of a pollutant solution. The reaction mixture is subjected to irradiation from a 500 W UV mercury lamp (with a dominant wavelength of 265 nm and the light source located 10 cm away from the test tube), with samples collected at five-minute intervals. These samples undergo centrifugation at 8000 rpm for 10 min, after which the residual concentration of salicylic acid in the supernatant is quantified using a UV-visible spectrophotometer at its characteristic wavelength of 297 nm. Concurrently, alterations in the spectral properties of the sample solution are documented for further analysis. The percentage removal of the pollutant is subsequently calculated using the appropriate formula:

$$\text{SA degradation rate}(\%) = (C_0 - C)/C_0 \times 100\% \quad (1)$$

where $C_0$ denotes the SA concentration measured before the reaction in mg/L, and C denotes the SA concentration measured after the reaction in mg/L.

Disodium ethylenediaminetetraacetic acid (EDTA), p-benzoquinone (BQ), and isopropyl alcohol (IPA) were employed as scavengers to capture reactive species, including holes (h+), superoxide anions ($\bullet O_{2^-}$), and hydroxyl radicals (•OH). In the photocatalysis experiments, solutions of SA were prepared with varying quenchers. The reactions were conducted in the dark for a duration of 60 min to establish an equilibrium between adsorption and desorption processes. Following this period, the reaction mixtures were subjected to irradiation with a 500 W UV mercury lamp. The samples underwent centrifugation at 8000 rpm for 10 min, after which the concentration of SA remaining in the supernatant was quantified using a UV-visible spectrophotometer at a wavelength of 297 nm. This procedure was implemented to elucidate the different types of active species involved in the photocatalytic reaction.

## 3. Results and Discussions

### *3.1. Analysis of XRD and TEM-EDS Characterization Results of Ag-Doped Molecularly Imprinted $TiO_2$*

Figure 1 illustrates several overlapping XRD diffraction peaks between MIP-Ag-$TiO_2$ and Ag-$TiO_2$ within the 20° to 90° range. When plotting the absorption peaks from the PDF#21-1272 standard anatase colorimetric card as dashed lines and comparing them with the XRD patterns of MIP-$TiO_2$ and $TiO_2$, it is evident that both exhibit consistent XRD diffraction peaks on the {101}, {004}, {105}, and {211} crystal planes, indicating that the primary component is anatase [14]. Additionally, MIP-$TiO_2$ and $TiO_2$ display peaks on the {110} crystal plane, suggesting that some anatase has converted to the rutile phase [15,16]. The findings indicate that silver doping significantly retards the transformation of anatase into the rutile phase in MIP-$TiO_2$. Ag-related diffraction peaks are not seen in XRD, which may be due to the fact that Ag is doped at 1%, which is lower than 5% and difficult to recognize. According to the calculation results of JADE 6.0 software, the calculated grain sizes of $TiO_2$, MIP-$TiO_2$, Ag-$TiO_2$, and MIP-Ag-$TiO_2$ are 39.38 nm, 37.33 nm, 29.12 nm, and 21.61 nm, respectively. MIP-Ag-$TiO_2$ has the smallest grain size, and it is close to 20 nm, so it has a better nano-size effect.

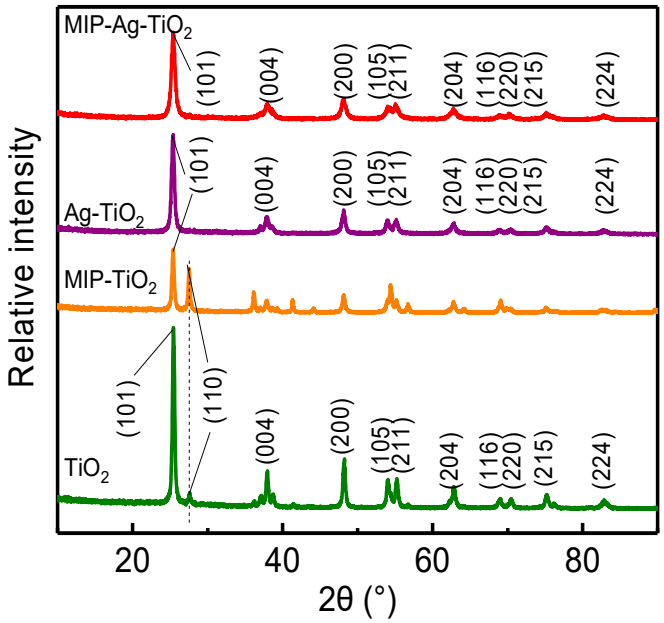



**Figure 1.** XRD patterns of different catalysts. ($TiO_2$, MIP-$TiO_2$, Ag-$TiO_2$, and MIP-Ag-$TiO_2$ are green, orange, purple, and red lines, respectively).

As shown in Figure 2a–c, the morphology of MIP-Ag-$TiO_2$ was examined using transmission electron microscopy (TEM), revealing that the material consists of nanoparticles interconnected within a size range of 200 nm. Figure 2b presents the statistical size distribution of 100 randomly chosen particles from Figure 2a, indicating that the catalyst particles predominantly have diameters between 10 and 40 nm. This suggests a nano-restricted domain effect that enhances the catalytic reaction's efficiency [17,18]. Additionally, the TEM-EDS mapping shown in Figure 2d–g indicates a uniform distribution of the elements Ti, O, and Ag on the catalyst's surface, aligning with the profiles observed in the original TEM images and corroborating the findings from the XRD analysis.

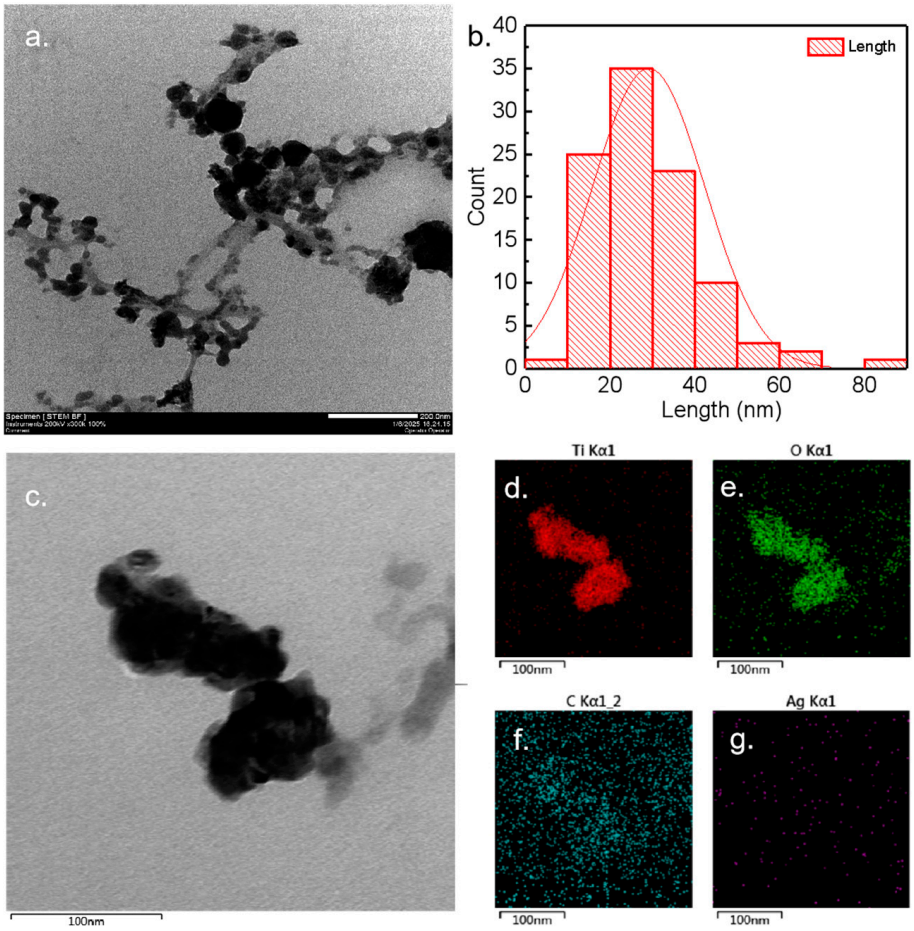



**Figure 2.** (**a**) TEM image of MIP-Ag-$TiO_2$. (**b**) Corresponding particle size distribution, the red line is a plot of the fitted change in trend. (**c**) TEM image at 100 nm and corresponding EDS scans (**d**–**g**).

### *3.2. Performance Analysis of Different Catalysts for SA Degradation*

To assess the material's adsorption capacity, adsorption isothermal experiments were conducted in the dark before the photocatalytic reaction, with the results presented in Figure 3a. The findings indicated that various photocatalysts achieved adsorption equilibrium within 30 min, revealing a limited dark adsorption effect. This can be attributed to the catalysts' lower adsorption capacity and quicker desorption rates. A high adsorption capacity could lead to the catalyst being surrounded by organic matter, which would disrupt the reaction's continuity [19,20]. In contrast, weaker and faster adsorption characteristics are more beneficial for maintaining an effective photocatalytic reaction. The physical and chemical adsorption of SA by $TiO_2$, MIP-$TiO_2$, Ag-$TiO_2$, and MIP-Ag-$TiO_2$ was minimal under stable pH and temperature conditions, leading to the decision not to conduct further dark adsorption tests in upcoming experiments.

In Figure 3b, it is evident that the four photocatalysts—$TiO_2$, MIP-$TiO_2$, Ag-$TiO_2$, and MIP-Ag-$TiO_2$—achieved degradation rates of 49.12%, 63.51%, 94.04%, and 98.60% of SA within 30 min, respectively. The findings indicate that the catalytic performance of silver-doped $TiO_2$ was significantly improved following surface modification. This improvement is likely linked to the unique spatial structure, the presence of numerous specific functional groups, the distinctive mesoporous structure, and the increased specific surface area of MIP-Ag-$TiO_2$ [21]. Furthermore, an optimal level of Ag doping can effectively capture holes on the $TiO_2$ surface, thereby reducing the recombination of photogenerated carriers and further boosting photocatalytic activity [22,23].

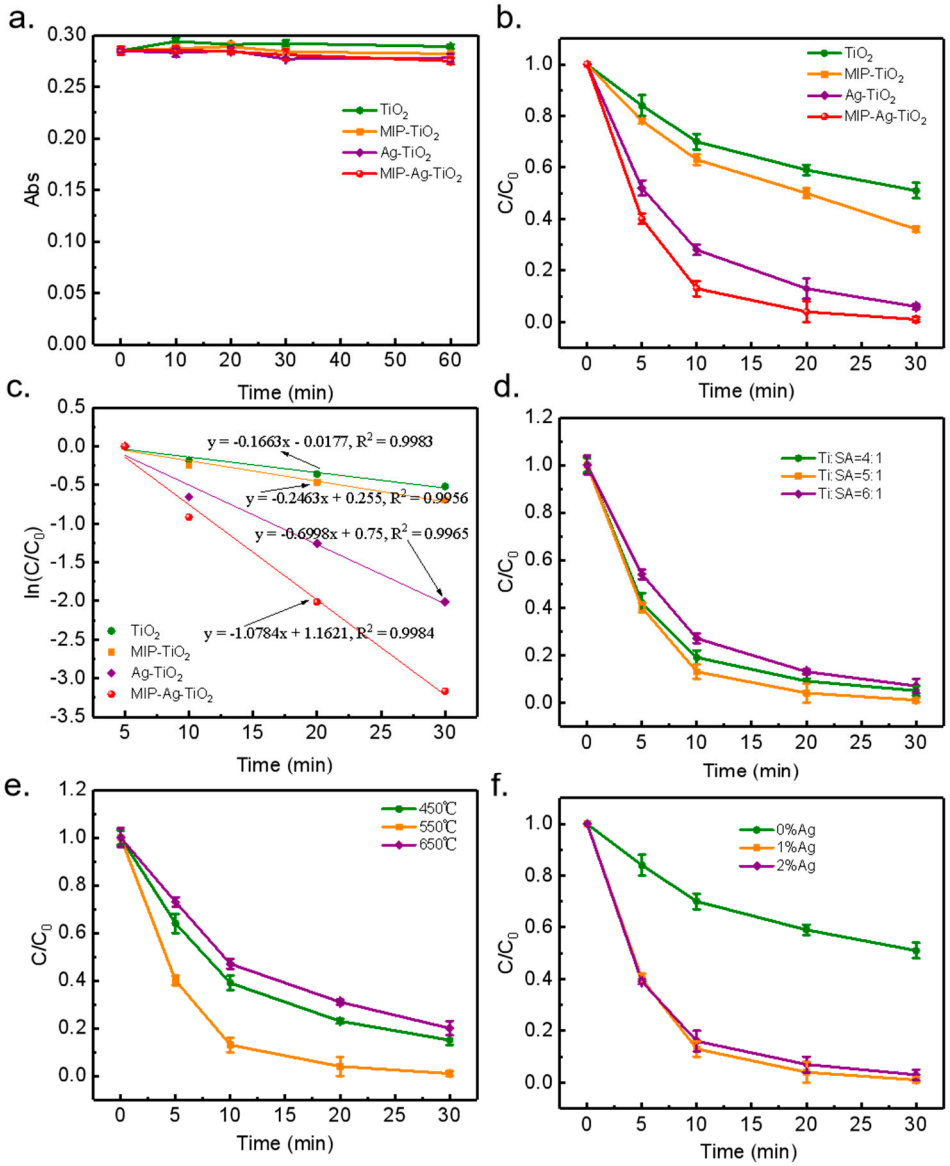



**Figure 3.** (**a**) Adsorption properties of the materials (stirring the reaction in the dark); (**b**) degradation properties of SA with different catalysts; (**c**) kinetic analysis; (**d**) effect of template molecular weight; (**e**) effect of calcination temperature; (**f**) effect of calcination time.

As shown in Table 1, the fitted $R^2$ values of the first-stage reaction kinetics of the four catalysts were all greater than 0.9 or above, which exhibited better fitting results, indicating that they all conformed to the photocatalytic first-stage reaction kinetics. Figure 3c shows that the absolute values of the rate constants for $TiO_2$ and MIP-$TiO_2$ are relatively close to each other, at 0.1663 and 0.2463, respectively. The rate constant for MIP-Ag-$TiO_2$ is significantly higher, at 0.6998, which is an enhancement of 3.2-fold with respect to $TiO_2$.

As shown in Figure 3d–f, the effects of different influencing factors on the performance of the photocatalysts were explored according to the principle of the controlled variable method. The results showed that the optimal degradation rate of SA reached 98.6% when the molar ratio of tetra-n-butyl titanate to the template molecule was 5:1, the calcination temperature was 550 °C (2 h), and the doping amount of Ag was 1% (molar ratio). The photocatalytic performance of the catalysts exhibited an initial increase followed by a decrease as the amount of Ag doping varied, with the highest performance observed at 1% doping. This indicates that the photocatalytic efficiency of MIP-Ag-$TiO_2$ is significantly influenced by different levels of Ag doping under consistent calcination temperature

conditions. Variations in Ag amounts may alter the catalysts' microstructure and phase distributions, which can greatly impact their catalytic performance. Additionally, the quantity of imprinted molecules is crucial to the photocatalytic characteristics of MIP-Ag-$TiO_2$. Different molecular weights of these imprinted molecules can modify the number of selectively recognized active sites on the catalyst's surface, thereby influencing its catalytic effectiveness [24].

**Table 1.** First-order reaction kinetic fitting results of different catalysts for photocatalytic degradation of SA in 30 min.

| Serial No. | Catalysts | Pollutant | Absolute Value of Rate Constant K | Fitting Formula | $R^2$ |
|---|---|---|---|---|---|
| 1 | $TiO_2$ | SA | 0.1663 | $y = -0.1663x - 0.0177$ | 0.9983 |
| 2 | MIP-$TiO_2$ | SA | 0.2463 | $y = -0.2463x + 0.255$ | 0.9956 |
| 3 | Ag-$TiO_2$ | SA | 0.6998 | $y = -0.6998x + 0.750$ | 0.9965 |
| 4 | MIP-Ag-$TiO_2$ | SA | 1.0784 | $y = -1.0784x + 1.1621$ | 0.9984 |

In Figure 4a–d, it can be seen that the particles of $TiO_2$, MIP-$TiO_2$, Ag-$TiO_2$, and MIP-Ag-$TiO_2$ are at the nanoscale but show a degree of agglomeration. As can be seen from the SEM, the material appears micron-sized (>3 microns). This level of agglomeration may be closely linked to the challenges in controlling the morphology during its synthesis [25,26].

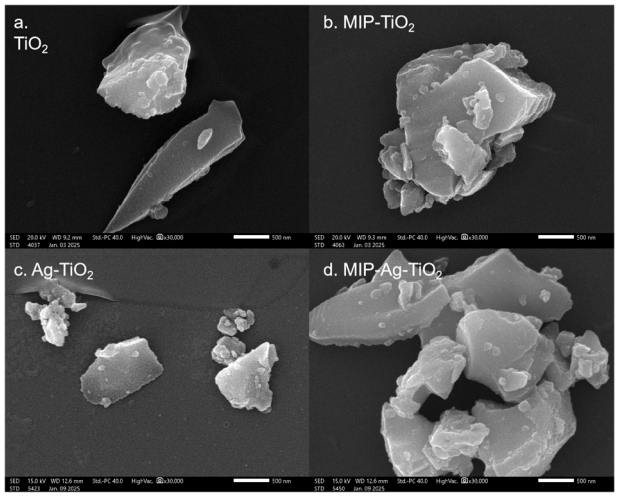



**Figure 4.** SEM images of different catalysts: (**a**) $TiO_2$; (**b**) MIP-$TiO_2$; (**c**) Ag-$TiO_2$; (**d**) MIP-Ag-$TiO_2$.

There is a clear relationship between the nano-size effect of MIP-Ag-$TiO_2$ and its specific surface area, which is why BET specific surface area characterization experiments were conducted in this research. Figure 5 illustrates the nitrogen adsorption–desorption curves for $TiO_2$, MIP-$TiO_2$, Ag-$TiO_2$, and MIP-Ag-$TiO_2$. The data show that all four catalysts exhibit a distinct H3-type adsorption hysteresis loop, indicating a significant presence of mesoporous structures within these materials [27]. Based on IUPAC classification for mesoporous materials, all of them fit the characteristics of a Langmuir-type IV curve, confirming their classification as mesoporous materials [28,29]. By integrating the results from XRD analysis with observations from photocatalytic experiments, it can be inferred that smaller grain sizes correlate with enhanced photocatalytic activity. Since MIP-Ag-$TiO_2$ has a smaller grain size and a larger specific surface area compared to $TiO_2$, its ability to adsorb pollutant molecules is significantly improved, thereby boosting its effectiveness in the photocatalytic degradation of organic matter.

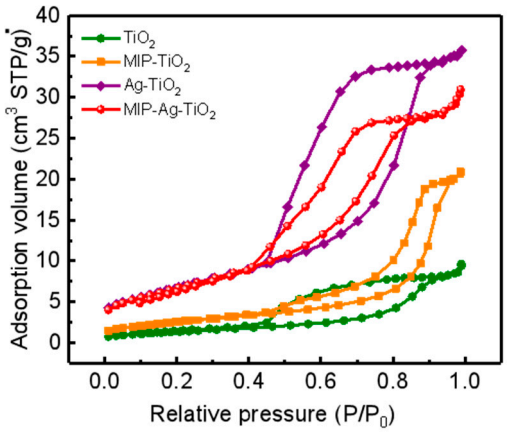



**Figure 5.** $N_2$ adsorption–desorption profile.

Meanwhile, the BET specific surface areas of the four catalysts were 5.04 $m^2/g$, 9.29 $m^2/g$, 24.73 $m^2/g$, and 24.67 $m^2/g$, respectively, and the results showed that Ag doping significantly increased the specific surface area of $TiO_2$, and this improvement helped to enhance its photocatalytic performance. The specific surface area of MIP-Ag-$TiO_2$ (24.67 $m^2/g$) was significantly enhanced compared with that of pure $TiO_2$ (5.04 $m^2/g$), and its mesoporous structure (average pore size of 7.03 nm) matched with the size of pollutant molecules, which enhanced the adsorption capacity and mass transfer efficiency. Combined with the XRD results, the decrease in grain size and the increase in specific surface area together increased the density of surface active sites, promoting the effective utilization of photogenerated carriers. In addition, the multiple light scattering effect of the mesoporous structure enhances the light trapping ability, which synergistically optimizes the charge separation efficiency and ultimately achieves the enhancement of the degradation performance.

XPS analysis provides a detailed examination of the surface elemental composition and charge states of the synthesized catalysts. Figure 6a–f present the XPS spectra for MIP-Ag-$TiO_2$ compared to $TiO_2$. The spectra reveal that MIP-Ag-$TiO_2$ exhibits an additional characteristic absorption peak for Ag, indicating successful doping of Ag into MIP-Ag-$TiO_2$. Additionally, as illustrated in Figure 6a, both catalysts show significant elemental C signals in their full XPS spectra, likely due to the introduction of elemental C for instrument calibration during testing. The elemental content analysis in Figure 6f indicates that the atomic percentages of Ti, Ag, O, and C in MIP-Ag-$TiO_2$ are 25.92%, 0.89%, 52.26%, and 20.93%, respectively, while $TiO_2$ has atomic proportions of Ti, O, and C at 24.33%, 49.55%, and 26.12%. These findings not only confirm the successful doping of Ag but also provide crucial data on elemental distribution for optimizing catalyst performance and further understanding their potential photocatalytic activities. Ag 3D high-resolution spectra show binding energies located at 367.8 eV (Ag 3d5/2) and 373.8 eV (Ag 3d3/2), indicating that silver coexists in a metallic state ($Ag^0$) and a small amount in an oxidized state ($Ag_2O$). The localized surface plasmon resonance effect of the $Ag^0$ nanoparticles significantly enhances the visible absorption (as confirmed by the UV-Vis DRS redshift), while the surface $Ag_2O$ can act as an electron trap to promote the migration of photogenerated electrons from the $TiO_2$ conduction band to Ag and inhibit carrier complexation (62% reduction in PL intensity). In addition, Ag doping led to a negative shift of the Ti 2p binding energy by 0.3 eV (Figure 6c), indicating that the increased electron density on the $TiO_2$ surface, together with the oxygen vacancy formation (531.5 eV peak enhancement in the O 1s spectra), optimized the interfacial charge transfer efficiency and ultimately

synergistically enhanced the photocatalytic degradation activity (3.2-fold enhancement in SA degradation rate).

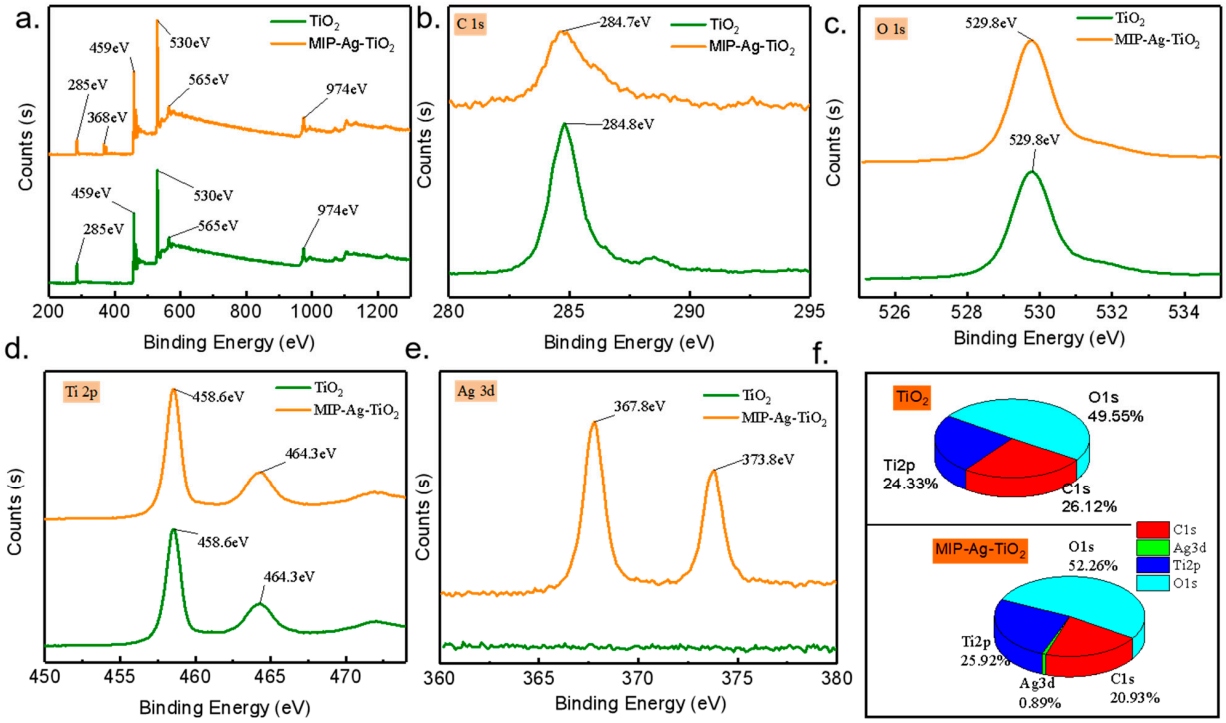



**Figure 6.** (**a**) Full XPS spectra of different catalysts; magnified XPS spectra: (**b**) C 1s, (**c**) O 1s, (**d**) Ti 2p, (**e**) Ag 3d; (**f**) atom ratio data of different catalysts.

The FT-IR spectral analysis shown in Figure 7 indicates that the spectra of the four catalysts remained largely unchanged, suggesting that the SA molecules were completely eliminated after elution, leaving no residual organic groups on the surface of MIP-Ag-$TiO_2$. Notably, there were no vibrational absorption peaks in the 3000 to 3300 $cm^{-1}$ range, further confirming the absence of intact SA molecules in MIP-Ag-$TiO_2$. This finding is essential for evaluating the catalyst's purity and removal efficiency. Additionally, the absorption peaks in the 500–1000 $cm^{-1}$ range of MIP-Ag-$TiO_2$ increased with higher SA concentrations, indicating a strengthened interaction through hydrogen bonds. This suggests that the presence of SA enhances the selective recognition of target pollutants by MIP-Ag-$TiO_2$, potentially boosting its photocatalytic degradation efficiency of SA. Thus, the FT-IR analysis not only validated the successful removal of SA but also highlighted how varying SA concentrations improved the catalyst's recognition and degradation capabilities, providing a significant foundation for the advancement of more effective photocatalytic materials.

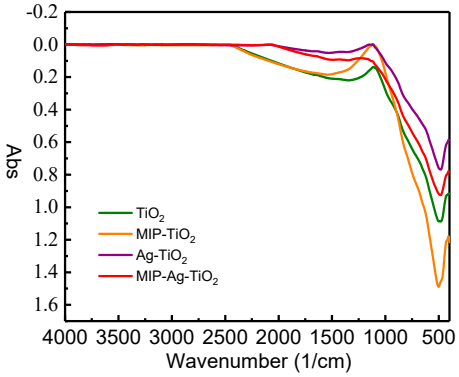



**Figure 7.** FT-IR plots of different catalysts.

### *3.3. Photocatalytic Selectivity and Recyclability Analysis*

To assess the selectivity of the catalysts, we selected phenol, which has a similar structure to the target pollutant SA, as a reference. $TiO_2$ was used as a control catalyst to examine the degradation effects of various catalysts on both SA and phenol, with the results presented in Figure 8a. We define the selectivity coefficient R as the ratio of the kinetic rate constant of the target pollutant to that of the comparison pollutant. Furthermore, the ratio of the selectivity coefficient of the target catalyst to that of the control catalyst is termed the selectivity factor $\alpha$.

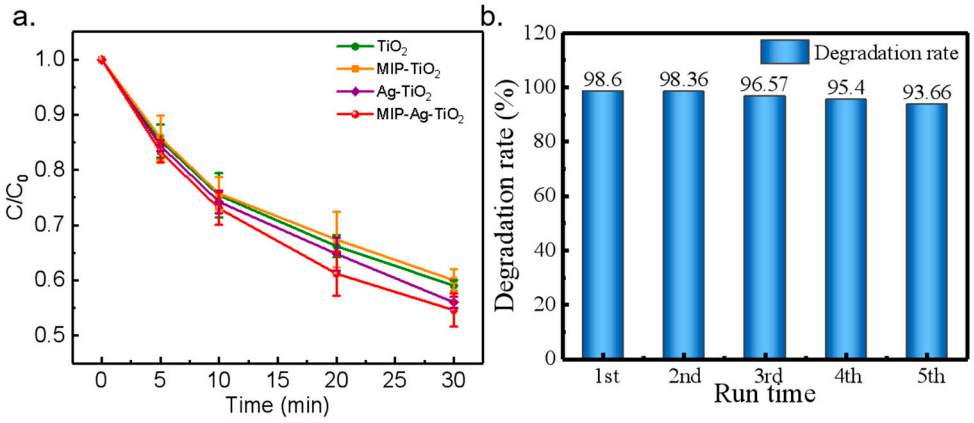



**Figure 8.** (**a**) Degradation of phenol by different catalysts. (**b**) Reuse experiment with MIP-Ag-$TiO_2$.

The selectivity coefficient R and selectivity factor $\alpha$ were used to examine the selectivity of the catalysts. They were calculated as follows, respectively [30]:

$$R = K_1/K_2 \quad (2)$$

$$\alpha = R_{MIP}/R_{NIP} \quad (3)$$

where $R$ and $\alpha$ denote the selectivity coefficient and selectivity factor, respectively; $K_1$ and $K_2$ denote the kinetic parameters of the first-stage reaction for the degradation of target and non-target pollutants, respectively; and $R_{MIP}$ and $R_{NIP}$ denote the selectivity coefficients of molecularly imprinted (*MIP*) and non-molecularly imprinted (*NIP*) catalysts, respectively.

In assessing the photocatalytic efficiency of $TiO_2$, we found that the kinetic rate constants for the first-order reactions in the degradation of SA and phenol were 0.166 and 0.131, respectively. This information enabled us to determine a selectivity coefficient R of 1.272, indicating that the catalyst exhibits a degree of selectivity towards SA. This finding implies that $TiO_2$ can preferentially break down this specific pollutant.

The test results for MIP-$TiO_2$ indicated a selectivity coefficient R of 1.950, demonstrating some selectivity in the degradation of SA. In contrast, MIP-Ag-$TiO_2$ exhibited a selectivity coefficient R of 7.128, which is 3.66 times greater than that of MIP-$TiO_2$. This notable enhancement suggests that the addition of silver enhances the selectivity of MIP-$TiO_2$, giving MIP-Ag-$TiO_2$ a greater capacity for degrading SA.

Moreover, the selectivity factor $\alpha$ of MIP-Ag-$TiO_2$ was measured at 5.645, significantly exceeding the threshold of 2 (see Table 2). This finding reinforces the notion that MIP-Ag-$TiO_2$ exhibits considerable selectivity for SA, suggesting its superior effectiveness in addressing particular pollutants. Overall, these results demonstrate that MIP-Ag-$TiO_2$ not only has high selectivity but also significantly improves the degradation efficiency of SA, thereby strongly supporting its use in environmental remediation.

**Table 2.** Comparison of kinetic constants and selectivity calculations for different catalysts.

| No. | Catalysts | Time | \|k\| Value | | R Value | $\alpha$ Value |
|---|---|---|---|---|---|---|
| | | | SA | Phenol | | |
| 1 | $TiO_2$ | 30 min | 0.166 | 0.131 | 1.272 | 1.000 |
| 2 | MIP-$TiO_2$ | 30 min | 0.246 | 0.126 | 1.950 | 1.544 |
| 3 | Ag-$TiO_2$ | 30 min | 0.700 | 0.142 | 4.914 | 3.892 |
| 4 | MIP-Ag-$TiO_2$ | 30 min | 1.078 | 0.151 | 7.128 | 5.645 |

When the substances on the catalyst surface are not strongly chemisorbed, catalyst activity can typically be restored through simple water washing. However, if chemisorption or strong physisorption occurs, it may be necessary to use acid or alkali washing or other regeneration techniques to regain activity. In this research, MIP-Ag-$TiO_2$ demonstrated a low adsorption capacity, indicating that it did not establish a strong physical or chemical bond with SA. Consequently, the research team evaluated the reusability of the MIP-Ag-$TiO_2$ catalyst by washing and drying it, with the results presented in Figure 8b.

The test results clearly show that the degradation rate of MIP-Ag-$TiO_2$ only decreased by 4.94% after being reused five times (Figure 8b). This suggests that MIP-Ag-$TiO_2$ has excellent reusability for the photocatalytic degradation of SA pollutants. Its sustained catalytic performance not only enables the catalyst to remain highly efficient during repeated use but also helps lower operating costs and enhance economic efficiency in real-world applications. Consequently, the outstanding performance of MIP-Ag-$TiO_2$ indicates significant potential for application and promising prospects in the field of photocatalysis.

### *3.4. Effect of pH and Analysis of TOC Results*

Based on the mineralization data of total organic carbon (TOC) during photocatalytic degradation (Figure 9a), the mineralization efficiencies of the four groups of catalysts showed obvious gradient differences within 2 h. The mineralization efficiencies of the four groups of catalysts were significantly higher than those of the commercial P25 $TiO_2$. The commercial P25 $TiO_2$ exhibited a mineralization rate of 68.43%, which was significantly higher than that of normal $TiO_2$ (58.85%), attributed to its optimized anatase/rutile heterojunction structure, which could effectively inhibit photogenerated carrier complexation. The Ag nanoparticle-modified Ag-$TiO_2$ system elevated the mineralization rate to 69.56%. Notably, the significant enhancement of the mineralization rate over the simple degradation rate (a 10–15% gap usually exists in the literature) indicates that the system not only destroys the SA molecular structure but also further oxidizes the intermediates (e.g., benzene ring-opening products, short-chain carboxylic acids, etc.) to $CO_2$ and $H_2O$, which is attributed to the multi-stage pore structure in MIP-Ag-$TiO_2$.

As shown in Figure 9b, the degradation efficiency of salicylic acid (SA) by the MIP-Ag-$TiO_2$ photocatalytic system showed a significant dependence on the solution pH. The removal of SA was enhanced from 97.81% to 98.6% in the range of strong to weak acidity (pH = 3~5), which reached the optimal reaction interval. This phenomenon can be attributed to the dynamic regulation of the charge state on the surface of the photocatalyst: when the pH is close to the isoelectric point of $TiO_2$ (pHpzc $\approx$ 6.2), the degree of protonation on the surface of the catalyst is increased, and the positively charged surface is more likely to adsorb the carboxylate anionic form of SA through electrostatic interaction (SA exists in the form of $C_6H_4(OH)COO^-$ at pH > 2.9), thus enhancing the interfacial mass transfer efficiency. Meanwhile, the acidic environment is beneficial to maintain the stability of Ag nanoparticles and avoid their oxidative deactivation, and $H^+$ as a trapping agent for holes ($h^+$) can inhibit the complexation of photogenerated carriers and promote the generation of -OH radicals.

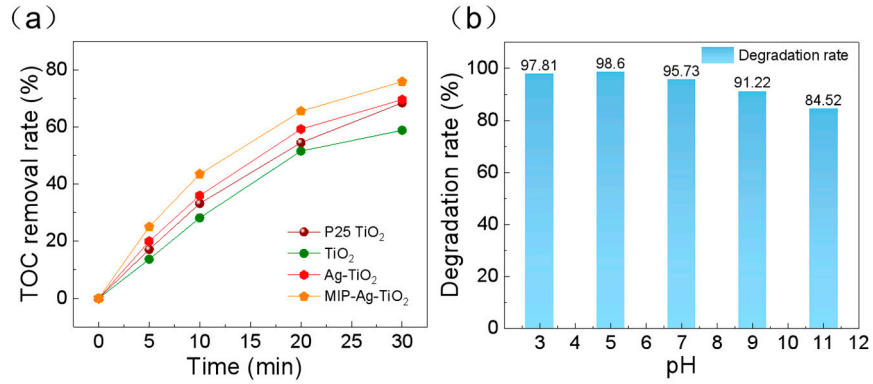



**Figure 9.** (**a**) Analysis of the change in TOC degradation rate during SA degradation by different catalysts (including P25 $TiO_2$); (**b**) degradation performance of catalysts for SA under different pH conditions.

However, the degradation efficiency decreased significantly from 95.73% to 84.52% when the solution was shifted to neutral to weakly alkaline conditions (pH = 7~11). This change involves multiple inhibitory mechanisms: first, the enhanced hydroxylation of the catalyst surface leads to increased electrostatic repulsion with SA anions and a decrease in the specific adsorption capacity; second, Ag may be partially converted to $Ag_2O$ under a high pH or may form [Ag(O)] with OH to in turn form [$Ag(OH)_2$]-complexes, weakening its surface plasmon resonance effect; in addition, alkaline conditions alter the generation path of reactive oxygen species, and the superoxide radical ($-O_2^-$) is blocked by protonation ($-O_2^- + H^+ \rightarrow HO_2^-$, pKa ≈ 4.8), leading to a decrease in their oxidizing capacity. Notably, deprotonation of SA molecules may occur at pH > 9 to generate bis-negative ions ($C_6H_4$(O-)COO-), whose spatial site-barrier effect with the catalyst surface and electron cloud repulsion further inhibit the degradation kinetics. This pH-responsive property differs from the behavior of typical $TiO_2$-based photocatalysts reported in the literature and may originate from the modulation effect of the molecularly imprinted layer (MIP): the three-dimensional cavity structure of MIP enhances the recognition and adsorption of SA through hydrogen bonding and π–π interactions under acidic conditions, whereas deactivation of the binding sites occurs due to deprotonation of the functional groups in alkaline environments. This finding provides important guidance for practical wastewater treatment—by preadjusting the pH of the system to weakly acidic (pH ≈ 5), the surface properties of the catalyst, the pollutant adsorption efficiency, and the kinetics of radical generation can be optimized simultaneously to maximize the degradation efficacy.

### *3.5. Quenching Experiments and Analysis of EPR Results*

In the field of photocatalytic degradation, it is crucial to deeply investigate the influence of active substances on the degradation efficiency. Taking the process of MIP-Ag-$TiO_2$ photocatalytic degradation of SA wastewater as an example, we can obtain key information from the experimental data and characterization analysis. From the experimental results in Figure 10a, it can be seen that the degradation rate of SA by MIP-Ag-$TiO_2$ showed significant changes when isopropanol, EDTA, and p-benzoquinone were added to the reaction system, respectively. The degradation rate was as high as 98.6% when these substances were not added, while it decreased to 68.36% after the addition of isopropanol, became 72.23% after the addition of EDTA, and was 82.15% after the addition of p-benzoquinone. Since isopropanol was mainly used to capture •OH, EDTA was used to capture $h^+$, and p-benzoquinone was used to capture $\bullet O_2^-$; the significant decrease in the degradation rate indicated that during the photocatalytic degradation of SA wastewater by MIP-Ag-$TiO_2$, three active substances, •OH, $h^+$, and $\bullet O_2^-$, were involved in the reaction, and judging

from the decrease in the degradation rate, the main active substance was likely •OH, followed by $h^+$ and $•O_{2^-}$.

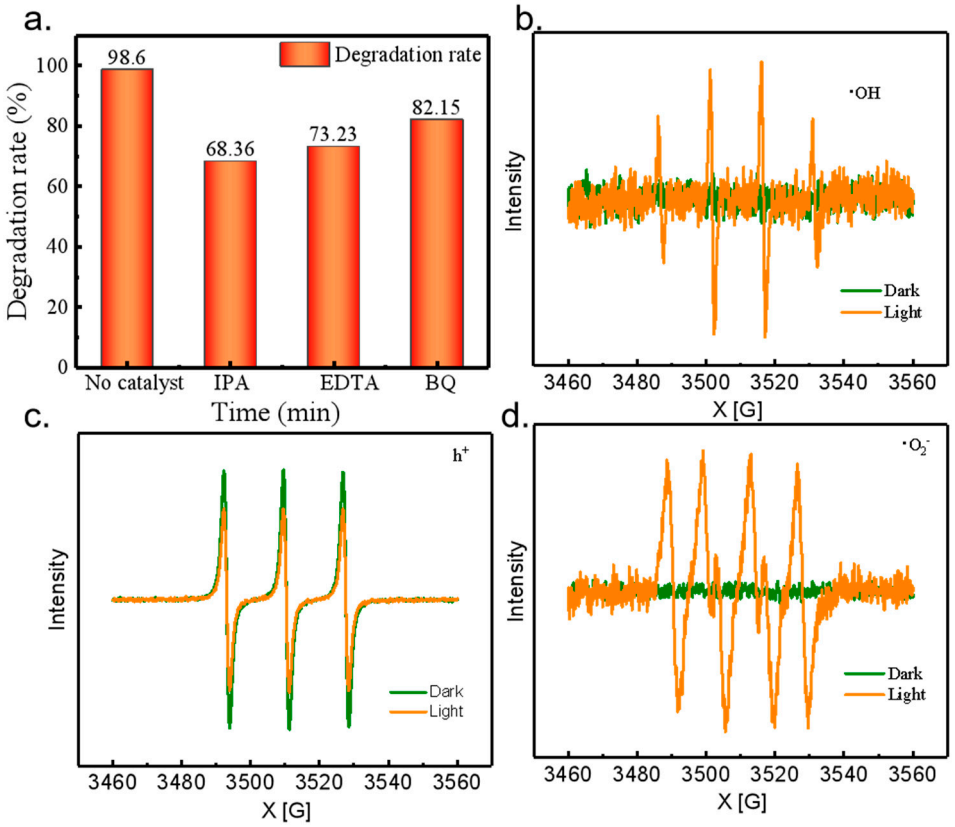



**Figure 10.** (**a**) Quenching experiments; characterization of EPR, (**b**) •OH, (**c**) h+, (**d**) $•O_{2^-}$.

To further verify this conclusion, EPR characterization of MIP-Ag-$TiO_2$ was carried out (Figure 10b–d). From the characterization results, we can clearly observe that the photocatalytic system is able to produce $h^+$, •OH, and $•O_{2^-}$ continuously and stably. Three characteristic peaks of DMPO-•OH adduct, DMPO-$h^+$, and DMPO-$•O_{2^-}$ were detected after 15 min of UV lamp irradiation, a phenomenon that visually proves the presence of these three active substancs during the reaction process and that that they play a key role in the degradation of SA [31]. This result is highly consistent with the results of the previous quenching experiments, which further validates our inference based on the quenching experimental data. Hence, both the changes in degradation rate in the quenching experiments and the detection of characteristic peaks in the EPR characterization fully indicated that the three active substances, •OH, $h^+$, and $•O_{2^-}$, were indispensable in the photocatalytic degradation of SA wastewater by MIP-Ag-$TiO_2$. This research result is of great significance for understanding the photocatalytic degradation mechanism of MIP-Ag-$TiO_2$, optimizing the photocatalytic reaction conditions, and improving the degradation efficiency of SA wastewater.

### *3.6. Comparison of Catalyst Performance from Different Studies*

A comprehensive comparison of the performance of different catalysts and of the results of the work with the results of others' research work allowed for fully exploring the water treatment performance of the photocatalysts. As can be seen from Table 3, the MIP-Ag-$TiO_2$ synthesized in this work has a relatively good photocatalytic effect on SA under UV light. Molecularly imprinted S-doped $TiO_2$ required 120 min to completely degrade SA under simulated sunlight, while the MIP-Ag-$TiO_2$ in the present work required

only 30 min. The catalytic efficiency of MIP-Ag-$TiO_2$ in the present work is the highest to date for the photocatalytic degradation of SA, which indicates that MIP-Ag-$TiO_2$ has great potential for application.

**Table 3.** Comparison of the photodegradation of SA in different research works.

| No. | Catalysts | Light Source | Additive Amount (g/L) | SA Concentration | Time (min) | Degradation Rate | Reference |
|---|---|---|---|---|---|---|---|
| 1 | MIP-S-$TiO_2$ | Simulation of sunlight | 1 | 20 mg/L | 120 | 71.89% | [32] |
| 2 | SA-$TiO_2$ | UV light | 1 | 10 mg/L | 30 | 62.69% | [24] |
| 3 | MIP-Bi-$TiO_2$ | UV light | 1 | 10 mg/L | 30 | 92.54% | [33] |
| 4 | MIP-Ag-$TiO_2$ | UV light | 1 | 10 mg/L | 30 | 98.6% | This work |

It is important to note that there are limitations in the direct degradation efficiency comparison between UV light (monochromatic high-energy photons) and simulated sunlight (broad spectrum including visible light), and that the conclusions of the present study centered on demonstrating the superior photon trapping ability of MIP-Ag-$TiO_2$ in the UV region. Follow-up studies will systematically evaluate its engineering applicability in the full spectrum as well as under actual sunlight.

## 4. Conclusions

This study investigated four photocatalysts—$TiO_2$, MIP-$TiO_2$, Ag-$TiO_2$, and MIP-Ag-$TiO_2$—for the photocatalytic degradation of SA (salicylic acid). Within 30 min, the degradation efficiencies were 49.12%, 63.51%, 94.04%, and 98.60%, respectively, with MIP-Ag-$TiO_2$ exhibiting the highest activity due to its highly active anatase structure. Bandgap measurements revealed that MIP-Ag-$TiO_2$ had the lowest bandgap (2.74 eV), enhancing electron transfer and light absorption, thereby improving photocatalytic performance. Ag doping significantly increased the specific surface area of $TiO_2$ (MIP-Ag-$TiO_2$: 24.67 $m^2/g$), further boosting catalytic activity. MIP-Ag-$TiO_2$ demonstrated exceptional selectivity for SA, with a selectivity coefficient (R) of 7.128, 3.66 times higher than that of MIP-$TiO_2$. Mechanistic studies identified •OH as the primary active species, followed by $h^+$ and $\bullet O_2^-$, providing critical insights into the photocatalytic mechanism and optimization of reaction conditions.

**Author Contributions:** X.L.: Reading and final approval of the version to be published. Y.L.: Data curation, validation, writing—original draft preparation, formal analysis, writing—reviewing and editing. All authors have read and agreed to the published version of the manuscript.

**Funding:** No funding or not able to provide at the moment.

**Data Availability Statement:** Data will be made available on request.

**Acknowledgments:** We also thank eceshi (www.eceshi.com) (accessed on 1 December 2024) for the characterization.

**Conflicts of Interest:** The authors declare no conflicts of interest.

## References

1. Zhao, L.; Liu, Y.; Xi, X.; Nie, Z.; Yee Lim, F.; Ong, S.L.; Hu, J. Design of dual-LSPR Bi/$W_{18}O_{49}$ composite and its red-light driven photocatalytic property in the photocatalytic degradation of PPCPs. *Chem. Eng. J.* **2024**, *481*, 148119. [CrossRef]
2. Rehman, M.U.; Nisar, B.; Yatoo, A.M.; Sehar, N.; Tomar, R.; Tariq, L.; Aldossari, R.M. After effects of Pharmaceuticals and Personal Care Products (PPCPs) on the biosphere and their counteractive ways. *Sep. Purif. Technol.* **2024**, *342*, 126921. [CrossRef]
3. Harmankaya, S.; Deveci, H.A.; Harmankaya, A.; Gül, F.H.; Atar, N.; Yola, M.L. Thiram determination in milk samples by surface plasmon resonance based on molecularly imprinted polymers and sulphur-doped titanium dioxide. *Biosensors* **2024**, *14*, 329. [CrossRef] [PubMed]

4. Kubiak, A.; Stachowiak, M.; Cegłowski, M. Unveiling the latest developments in molecularly imprinted photocatalysts: A state-of-the-art review. *Polymers* **2023**, *15*, 4152. [CrossRef]
5. Hutt, A.J.; Caldwell, J.; Smith, R.L. The metabolism of aspirin in man: A population study. *Xenobiotica* **1986**, *16*, 239–249. [CrossRef]
6. Hoa, N.T.; Bich, H.N.; Mechler, A.; Vo, Q.V. The hydroperoxyl radical scavenging activity of natural hydroxybenzoic acids in oil and aqueous environments: Insights into the mechanism and kinetics. *Phytochemistry* **2022**, *201*, 113281.
7. Gu, X.; Wang, X.; Zhu, L.; Han, Q.; Liu, Q. Preparation of N/La-$TiO_2$ and photocatalytic degradation of salicylic acid. *Environ. Sci. Technol.* **2020**, *43*, 104–109. (In Chinese)
8. Ferreira, V.R.A.; Pereira, C.M.; Silva, A.F.; Azenha, M.A. Ag-doped hollow $TiO_2$ microspheres for the selective photo-degradation of bilirubin. *Appl. Surf. Sci.* **2023**, *641*, 158457. [CrossRef]
9. Liu, Y.; Wang, L.; Li, H.; Zhao, L.; Ma, Y.; Zhang, Y.; Wei, Y. Rigorous recognition mode analysis of molecularly imprinted polymers—Rational design, challenges, and opportunities. *Prog. Polym. Sci.* **2024**, *150*, 101790. [CrossRef]
10. Arabzadeh, N.; Khosravi, A.; Mohammadi, A.; Mahmoodi, N.M. Enhanced photodegradation of hazardous tartrazine by composite of nanomolecularly imprinted polymer-nanophotocatalyst with high efficiency. *Desalin. Water Treat.* **2016**, *57*, 3142–3151. [CrossRef]
11. Geng, L.; Liu, J.; Zhang, W.; Wang, H.; Huang, J.; Wang, G.; Sun, X. Preparation of dual recognition adsorbents based on molecularly imprinted polymers and aptamer for highly sensitive recognition and enrichment of ochratoxin A. *J. Hazard. Mater.* **2024**, *476*, 135112. [CrossRef] [PubMed]
12. Wu, Y.; Li, Y.; Tian, A.; Mao, K.; Liu, J. Selective Removal of Perfluorooctanoic Acid Using Molecularly Imprinted Polymer-Modified $TiO_2$ Nanotube Arrays. *Int. J. Photoenergy* **2016**, *2016*, 7368795. [CrossRef]
13. Chen, X.; Liu, X.; Zhu, L.; Tao, X.; Wang, X. One-step fabrication of novel MIL-53(Fe, Al) for synergistic adsorption-photocatalytic degradation of tetracycline. *Chemosphere* **2022**, *291*, 133032. [CrossRef]
14. Bakhshizadeh, M.; Sazgarnia, A.; Seifi, M.; Hadizadeh, F.; Rajabzadeh, G.; Mohajeri, S.A. $TiO_2$-based mitoxantrone imprinted poly (methacrylic acid-co-polycaprolctone diacrylate) nanoparticles as a drug delivery system. *Curr. Pharm. Des.* **2017**, *23*, 2685–2694. [CrossRef] [PubMed]
15. Hanaor, D.A.; Sorrell, C.C. Review of the anatase to rutile phase transformation. *J. Mater. Sci.* **2011**, *46*, 855–874. [CrossRef]
16. Zhu, S.C.; Xie, S.H.; Liu, Z.P. Nature of rutile nuclei in anatase-to-rutile phase transition. *J. Am. Chem. Soc.* **2015**, *137*, 11532–11539. [CrossRef] [PubMed]
17. Zhang, J.; Cai, D.; Li, Z. Enhanced Electrocatalytic Performances by Spatially Confined Aqueous Electrolytes. *ChemistrySelect* **2024**, *9*, e202303285. [CrossRef]
18. Han, Y.; Ren, X.; Wu, T.; Li, Y.; Ma, H.; Ru, Z.; Wei, Q. Effective enrichment of free radicals through nanoconfinement boosts electrochemiluminescence of carbon dots derived from luminol. *Angew. Chem.* **2024**, *64*, e202414073. [CrossRef]
19. Králik, M. Adsorption, chemisorption, and catalysis. *Chem. Pap.* **2014**, *68*, 1625–1638. [CrossRef]
20. Kung, H.H.; Ko, E.I. Preparation of oxide catalysts and catalyst supports—A review of recent advances. *Chem. Eng. J.* **1996**, *64*, 203–214. [CrossRef]
21. Yu., X.; Deng, J.; Liu, Y.; Jing, L.; Gao, R.; Hou, Z.; Zhang, Z.; Dai, H. Enhanced water resistance and catalytic performance of Ru/$TiO_2$ by regulating brønsted acid and oxygen vacancy for the oxidative removal of 1, 2-dichloroethane and toluene. *Environ. Sci. Technol.* **2022**, *56*, 11739–11749. [CrossRef] [PubMed]
22. Kanakaraju, D.; Kutiang, F.D.; Lim, Y.C.; Goh, P.S. Recent progress of Ag/$TiO_2$ photocatalyst for wastewater treatment: Doping, co-doping, and green materials functionalization. *Appl. Mater. Today* **2022**, *27*, 101500. [CrossRef]
23. Kang, S.; Hwang, J. rGO-wrapped Ag-doped $TiO_2$ nanofibers for photocatalytic $CO_2$ reduction under visible light. *J. Clean. Prod.* **2022**, *374*, 134022. [CrossRef]
24. Liu, X.; Xu, C.; Zhu, L.; Wang, X. Molecular imprinting produces high photoelectric effect facilitating the efficient photocatalytic degradation of salicylic acid by $TiO_2$. *React. Kinet. Mech. Catal.* **2022**, *135*, 529–537. [CrossRef]
25. Brunelli, A.; Pojana, G.; Callegaro, S.; Marcomini, A. Agglomeration and sedimentation of titanium dioxide nanoparticles (n-$TiO_2$) in synthetic and real waters. *J. Nanopart. Res.* **2013**, *15*, 1684. [CrossRef]
26. Teleki, A.; Wengeler, R.; Wengeler, L.; Nirschl, H.; Pratsinis, S.E. Distinguishing between aggregates and agglomerates of flame-made $TiO_2$ by high-pressure dispersion. *Powder Technol.* **2008**, *181*, 292–300. [CrossRef]
27. Musso, M.; Veiga, S.; De León, M.A.; Quevedo, A.; Bussi, J. Hydrogen production from pure and crude glycerol photoreforming using platinum supported on $TiO_2$ and N-$TiO_2$. *Mater. Lett.* **2024**, *357*, 135714. [CrossRef]
28. Zhu, W.; Kuang, J.; Wang, Z.; Tian, J. Optimal Structure and Photocatalytic Performance of $C_3N_4$@$TiO_2$ Composite by Controlling the Molar Ratio of Components. *Langmuir* **2024**, *40*, 16972–16980. [CrossRef]
29. Fazil, M.; Alshehri, S.M.; Mao, Y.; Ahmad, T. Enhanced photo/electrocatalytic hydrogen evolution by hydrothermally derived Cu-doped $TiO_2$ solid solution nanostructures. *Langmuir* **2024**, *40*, 4063–4076. [CrossRef]

30. Zhu, L.; Liu, X.; Wang, X.; Meng, X. Evaluation of photocatalytic selectivity of Ag/Zn modified molecularly imprinted $TiO_2$ by multiwavelength measurement. *Sci. Total Environ.* **2020**, *703*, 134732. [CrossRef]
31. Peng, K.; Liu, X.; Wu, X.; Yu, H.; He, J.; Chen, K.; Wang, X. Study on the preparation of molecularly imprinted $ZrO_2$-$TiO_2$ photo-catalyst and the degradation performance of hydroquinone. *Environ. Sci. Pollut. Res.* **2023**, *30*, 83575–83586. [CrossRef] [PubMed]
32. Wang, Z.; Liu, X.; Li, W.; Wang, H.; Li, H. Enhancing the photocatalytic degradation of salicylic acid by using molecular imprinted S-doped $TiO_2$ under simulated solar light. *Ceram. Int.* **2014**, *40*, 8863–8867. [CrossRef]
33. Liu, X.; Xu, C.; Zhu, L.; Xie, S.; Shen, S.; Wang, X. One-step facile synthesis of shell-pearl structured photocatalysts for efficient removal of selected PPCPs from wastewater. *J. Environ. Chem. Eng.* **2021**, *9*, 106758. [CrossRef]

**Disclaimer/Publisher's Note:** The statements, opinions and data contained in all publications are solely those of the individual author(s) and contributor(s) and not of MDPI and/or the editor(s). MDPI and/or the editor(s) disclaim responsibility for any injury to people or property resulting from any ideas, methods, instructions or products referred to in the content.